

**Identification of muscle necrosis in the  
*mdx* mouse model of Duchenne muscular  
dystrophy using three-dimensional optical  
coherence tomography**

Blake R. Klyen  
Thea Shavlakadze  
Hannah G. Radley-Crabb  
Miranda D. Grounds  
David D. Sampson

# Identification of muscle necrosis in the *mdx* mouse model of Duchenne muscular dystrophy using three-dimensional optical coherence tomography

Blake R. Klyen,<sup>a,\*</sup> Thea Shavlakadze,<sup>b</sup> Hannah G. Radley-Crabb,<sup>b</sup> Miranda D. Grounds,<sup>b</sup> and David D. Sampson<sup>a,c</sup>

<sup>a</sup>The University of Western Australia, School of Electrical, Electronic and Computer Engineering, Optical + Biomedical Engineering Laboratory, M018, 35 Stirling Highway, Crawley, Western Australia 6009, Australia

<sup>b</sup>The University of Western Australia, School of Anatomy and Human Biology, Skeletal Muscle Research Group, M309, 35 Stirling Highway, Crawley, Western Australia 6009, Australia

<sup>c</sup>The University of Western Australia, Centre for Microscopy, Characterisation and Analysis, M018, 35 Stirling Highway, Crawley, Western Australia 6009, Australia

**Abstract.** Three-dimensional optical coherence tomography (3D-OCT) was used to image the structure and pathology of skeletal muscle tissue from the treadmill-exercised *mdx* mouse model of human Duchenne muscular dystrophy. Optical coherence tomography (OCT) images of excised muscle samples were compared with co-registered hematoxylin and eosin-stained and Evans blue dye fluorescence histology. We show, for the first time, structural 3D-OCT images of skeletal muscle dystropathology well correlated with co-located histology. OCT could identify morphological features of interest and necrotic lesions within the muscle tissue samples based on intrinsic optical contrast. These findings demonstrate the utility of 3D-OCT for the evaluation of small-animal skeletal muscle morphology and pathology, particularly for studies of mouse models of muscular dystrophy.

© 2011 Society of Photo-Optical Instrumentation Engineers (SPIE). [DOI: 10.1117/1.3598842]

Keywords: optical coherence tomography; three-dimensional imaging; small-animal imaging; skeletal muscle; Duchenne muscular dystrophy; *mdx* mouse; necrotic lesion; Evans blue dye.

Paper 11022R received Jan. 12, 2011; revised manuscript received May 17, 2011; accepted for publication May 19, 2011; published online Jul. 11, 2011.

## 1 Introduction

Animal models are routinely used in pre-clinical research to understand the cause and progression of diseases and to evaluate potential therapies. Duchenne muscular dystrophy (DMD) is the most severe form of the human muscular dystrophies, occurring at a rate of 1 in 3600 to 6000 male births worldwide.<sup>1</sup> The disease is characterized by the progressive degeneration of skeletal and cardiac muscle tissue, eventually resulting in death from respiratory or cardiac failure.<sup>1,2</sup> It is caused by a mutation of a recessive gene located on the X-chromosome that codes for the sub-sarcolemmal protein dystrophin, which is vital for preserving mechanical integrity of the muscle fibers (myofibers).<sup>3</sup> Absence of a functional form of this protein results in a fragile membrane that is easily damaged, activating an inflammatory response that leads to myofiber necrosis.<sup>4-6</sup> Normally, this would lead to regeneration of new muscle tissue, but in DMD repeated cycles of muscle necrosis result in the progressive replacement of functional tissue with fibrous and fatty connective tissue. These large regions of necrotic myofibers, inflammatory cells, and fibrous and fatty connective tissue within the muscle are termed necrotic lesions.<sup>7</sup>

Pharmaceutical and nutritional interventions are currently being investigated as potential treatments for the disease, aimed at slowing the inflammatory response that precedes the loss

of functional muscle tissue.<sup>8-11</sup> The conventional method for assessing the effectiveness of these treatments is based on animal models of the disease, using the morphological analysis of histological sections of excised tissue samples under light microscopy.<sup>12</sup> While extremely valuable for evaluating the efficacy of potential treatments, this method necessitates the sacrifice of large numbers of animals. The preservation, sectioning and staining, and microscopic evaluation of tissues is very time-consuming and laborious, and precludes the (longitudinal) study of the same animal over multiple time points. It would be better to have a means of assessment that could be conducted over time without having to sacrifice the animal and remove its tissue. Ideally, this method would be minimally invasive, able to quickly obtain large volumes of data, and have sufficient resolution to detect the morphological features of interest.

A number of *in vivo* biomedical imaging modalities currently in use or being developed are aimed at providing routine imaging of whole animals or muscles without the need for tissue biopsy or animal sacrifice. Modalities currently being investigated for *in vivo* assessment of muscle tissue include: ultrasound;<sup>13,14</sup> magnetic resonance imaging (MRI);<sup>15-21</sup> confocal, multi-photon, and second-harmonic generation microscopy;<sup>22-24</sup> noninvasive near-infrared optical imaging;<sup>25</sup> and optical coherence tomography (OCT).<sup>26,27</sup>

Ultrasonography is suitable for the routine clinical assessment of muscle condition in human DMD patients due to its large penetration depth, but is unable to resolve individual myofibers, which have typical diameters in the range 30 to 50  $\mu\text{m}$

Address all correspondence to: Blake R. Klyen, Optical + Biomedical Engineering Laboratory, School of Electrical, Electronic and Computer Engineering M018, The University of Western Australia, 35 Stirling Highway, Crawley, Perth, Western Australia 6009 Australia; Tel: +61-8-6488-3813; Fax: +61-8-6488-1319; E-mail: bklyen@ee.uwa.edu.au.

for mice.<sup>28</sup> More recently, ultrasound has been used for the quantitative assessment of skeletal muscle tissue from mouse models of muscular dystrophy. It is able to differentiate dystrophic from healthy skeletal muscle in *ex vivo* samples,<sup>14</sup> measure the response of tissue to pharmacological treatment *in vivo*,<sup>13</sup> and discriminate in longitudinal *in vivo* studies between mouse models of DMD with varying severity of dystrotophology.

MRI can discriminate between healthy and dystrophic muscles of mice *in vivo* and chronologically follow the extent of tissue damage and repair, qualitatively in images<sup>15,19</sup> and quantitatively with MR spectroscopy.<sup>16</sup> Albumin-targeted MRI contrast agents, such as gadolinium, have been used to quantitatively study the permeability of myofibers in different models of dystrophy<sup>17</sup> and to improve the imaging resolution.<sup>18</sup> MRI has also been used in studies of the dystrophic dog model for pre-clinical assessment of therapeutic interventions.<sup>20,21</sup> The ability to conduct *in vivo* 3D tissue analysis of an individual animal over time is attractive. The performance of high-resolution systems ( $\sim 30$  to  $40 \mu\text{m}$ )<sup>29</sup> is approaching that required to image individual myofibers, but access, cost, and the long acquisition times of MRI remain challenges impeding the uptake of this imaging modality for studies of mouse models of DMD.

Confocal, multi-photon, and second harmonic<sup>23,24</sup> microscopies are able to resolve the individual myofibers, but generally require *ex vivo* tissue samples. Studies of muscle damage *in vivo* have been reported,<sup>22</sup> but are limited to a few hundred micrometers in penetration depth, and often rely on fluorescence signals from exogenous contrast agents. Noninvasive near-infrared imaging is another modality that has been used to study the dystrophic tissue of whole live mice *in vivo* over time,<sup>25</sup> but it is unable to image the individual myofibers due to limited resolution.

Optical coherence tomography is a nondestructive optical imaging technology that is able to generate 3D images of the spatially localized intensity of backscattered light, approaching micron resolution and with a penetration up to 2 mm in tissue.<sup>30,31</sup> We have previously demonstrated the ability of OCT to visually differentiate intact healthy muscle from regions of necrosis and inflammation in a surgical mouse model of skeletal muscle damage and inflammation.<sup>27</sup> We showed that individual myofibers could be imaged by OCT, and areas that displayed a characteristic cross-sectional fiber pattern correlated well with healthy skeletal muscle tissue in the co-located histology sections. In contrast, regions of tissue damage and inflammation had lost this characteristic myofiber pattern appearance in the OCT images. Further, when compared to healthy tissue at the same depth, areas of tissue damage and inflammation had a lower OCT signal strength and lower contrast.

Few other studies have investigated the utility of OCT imaging of muscle pathology. Pasquesi et al. used polarization-sensitive OCT to measure changes in the birefringence of the skeletal muscle of a downhill treadmill-exercised X-chromosome-linked muscular dystrophy (*mdx*) mouse model.<sup>26</sup> Changes in the birefringence calculated from OCT B-scans were attributed to disruption of the ultrastructure of the muscle in response to exercise and the underlying presence of the dystrophy disease state. Hucker et al. used OCT imaging in conjunction with fluorescence imaging of voltage-sensitive dyes to investigate the structure-function relationship of myocardium at depth.<sup>32</sup> They found a strong correlation between

velocity vectors of electrical conduction and the orientation of cardiac fibers, as determined by OCT, and that structural heterogeneities contributed to arrhythmias. While others have shown incidental structural OCT imaging of skeletal and cardiac muscles,<sup>27</sup> to date no studies have shown the utility of structural OCT imaging of skeletal muscle tissue for the study of muscular dystrophy. We test the hypothesis that OCT is capable of visualizing morphological features of interest and identifying necrotic lesions in skeletal muscle tissue of mouse models of muscular dystrophy based on intrinsic optical contrast.

In this paper, we present our findings of three-dimensional optical coherence tomography (3D-OCT) imaging of the skeletal muscle tissue from the *mdx* mouse model for human Duchenne muscular dystrophy.<sup>12</sup> We show that 3D-OCT is capable of imaging the large-scale morphology of *ex vivo* skeletal muscle tissue samples and identifying necrotic lesions within these large volumes ( $\text{mm}^3$ ) based on intrinsic optical contrast. We compare images obtained by 3D-OCT with co-located conventional histology using two staining techniques, hematoxylin and eosin (H&E) and Evans blue dye (EBD), to identify the necrotic lesions containing necrotic myofibers, cellular debris, inflammatory cells, and fibrous and fatty connective tissue. In the remainder of this paper, we describe the imaging procedure, animal model and exercise protocol, and injection of EBD for the visual identification of candidate regions of muscle for OCT imaging. We present co-registered photographs, OCT images, H&E histology, and EBD-fluorescence histology of skeletal muscle tissue samples taken from the limbs of *mdx* mice. Our results demonstrate that 3D-OCT is able to identify necrotic lesions in a mouse model of human muscular dystrophy.

## 2 Methods

### 2.1 Animal Model, Treadmill Exercise, and Evans Blue Dye Injection

Five male *mdx* (C57BL/10SnSc<sup>mdx/mdx</sup>) twelve-week-old mice were obtained from the Animal Resources Centre, Murdoch, Western Australia. All animal experiments were conducted in strict accordance with the guidelines of the National Health and Medical Research Council Code of Practice for the Care and Use of Animals for Scientific Purposes (2004) and the Animal Welfare Act of Western Australia (2002) and were approved by the Animal Ethics Committee at The University of Western Australia. All mice completed 30 min of horizontal treadmill running at 12 m/min, which has been found to increase the extent of dystrotophology.<sup>33,34</sup>

Immediately following exercise, mice were injected with 1% EBD (Sigma, St. Louis, Missouri) (w/v) in phosphate buffered saline (PBS) (pH 7.5) by intraperitoneal injection at a dose of 100  $\mu\text{L}$  per 10 g per body weight.<sup>35</sup> Prior to injection, the solution was sterilized by passage through a Millex-GP 0.22  $\mu\text{m}$  filter (Milipore, Bedford, Massachusetts) and stored at 4°C.<sup>7</sup> The injection of EBD is a proven technique for identifying the onset of muscle damage<sup>35</sup> as it binds to serum albumin and will only readily diffuse into myofibers with a permeable (leaky or necrotic) membrane.<sup>12</sup> The EBD-positive degenerating myofibers can be macroscopically identified by their dark blue staining, which reveals the severity and spatial location of the

muscle damage in the animal, and microscopically identified in frozen histology sections by their red fluorescence. We used the injection of EBD to help guide our 3D-OCT imaging.

Twenty four hours after treadmill running, mice were anaesthetized with 2% v/v Isoflurane (Bomac, Australia), N<sub>2</sub>O, and O<sub>2</sub> and sacrificed via cervical dislocation. Skeletal muscles from the hindlimb (tibialis anterior, gastrocnemus, quadriceps) and forelimb (triceps) were excised and placed in PBS on ice for transportation and subsequent *ex vivo* 3D-OCT imaging. A total of 12 muscle samples from five mice were imaged and underwent subsequent histological processing, described in detail below.

## 2.2 Optical Coherence Tomography Imaging

A time-domain OCT system was used to image the *ex vivo* mouse skeletal muscle tissue samples (Fig. 1). A 14-mW broadband light source operating at 1320 nm (DenseLight Semiconductors, Singapore) with a measured 3-dB bandwidth of 154 nm was coupled into a fiber-based Michelson interferometer. The optical path length was varied using a frequency-domain optical delay line (FD-ODL)<sup>36</sup> in the reference arm to achieve an A-scan rate of 500 Hz, with a measured axial resolution of  $\sim 8 \mu\text{m}$  in air and system sensitivity of 104 dB. Lateral scanning in one dimension ( $x$ ) was achieved by a galvanometer mirror and objective lens setup with an NA of 0.07 and measured lateral resolution of  $\sim 11 \mu\text{m}$  at the beam waist ( $1/e^2$  intensity of beam diameter). The third dimension ( $y$ ) was obtained by linear translation of the sample to capture sequential B-scans ( $x$ - $z$ ) at  $10 \mu\text{m}$  intervals along the  $y$ -axis. The interference signal between the back-scattered light from the sample and reference arms was measured using a dual-balanced photodiode (NewFocus, Santa Clara, California) and the resulting signal bandpass filtered and logarithmically demodulated before analog-to-digital conversion. Data acquisition and system control was performed through a data acquisition card (PCI-6111E, National Instruments, Austin, Texas) using custom designed software running in LabVIEW (version 6.0, National Instruments, Austin, Texas).

All *ex vivo* muscle samples were imaged over a 6 h period following animal sacrifice. The tissue samples were placed on

a glass imaging-slide and immersed in PBS to maintain hydration and index match between the sample and imaging-slide throughout 3D-OCT scanning. The samples were oriented with the muscle fibers perpendicular to the optical axis, so that the longitudinal sections of subsequent histology used for verification were aligned parallel to the *en face* ( $x$ - $y$ ) OCT imaging plane. This orientation was chosen as it did not require further sectioning of the sample and most closely resembles the imaging strategy that would be adopted in future *in vivo* 3D-OCT imaging. Those regions of the tissue that displayed the blue stain of accumulated EBD were selected for imaging and full volume 3D-OCT scans measuring  $3 \times 10 \times 2.3 \text{ mm}$  ( $x, y, z$ ) were acquired.

## 2.3 Histological Processing and Image Co-registration

Following imaging, samples were frozen in liquid nitrogen-cooled isopentane for histological processing. Longitudinal serial sections of  $8 \mu\text{m}$ -thickness were cut on a cryostat at discrete intervals throughout the depth of the tissue and mounted on glass slides. These sections were closely aligned parallel to the *en face* ( $x$ - $y$ ) plane of the 3D-OCT scans. At discrete levels throughout the sample volume, the first three cut sections were mounted on a single slide for subsequent H&E staining, while the next three cut sections were mounted on a separate slide for EBD-fluorescence imaging. This sectioning protocol was repeated at  $80\text{-}\mu\text{m}$  intervals throughout the depth of the frozen sample. High-resolution digital imaging of the large area ( $\sim 10 \times 10 \text{ mm}$ ) H&E-stained sections was performed by light microscopy at  $20\times$  magnification using an automated system (ScanScope XT, Aperio Technologies Inc., Vista, California).

Multiplanar formatting was applied to the 3D data sets using custom software to extract 2D *en face* OCT images ( $3 \times 10 \text{ mm}$ ) that optimally matched the histological sections. The visualization of *en face* images of the OCT data is preferred as the entire image plane is within constant focus and has similar intensity levels. The logarithmically demodulated OCT signal was displayed with an inverse gray scale colormap, in which black represents increased reflectivity, and contrast was adjusted to better identify anatomical features of interest. This scheme facilitated matching OCT images with the corresponding H&E-stained histology. *En face* OCT and H&E-microscopy images were co-registered by matching for depth and visually correlating structural features of interest.

Once a necrotic lesion had been identified in the 3D-OCT scan and verified by the corresponding H&E-histology, the adjacent EBD-fluorescence sections were imaged to identify EBD accumulation in permeable myofibers. Fluorescence imaging was performed on a fluorescence microscope (Leica DM RB/E, Leica Microsystems, Wetzlar, Germany) with a green wavelength filter set (excitation filter BP 515–560 and emission LP 590) at a  $10\times$  magnification and with digital image capture (SciTech Q Imaging MicroPublisher 3.3 RTV). Nonoverlapping images of the entire cross-sectional area of the longitudinal sections were formed by tiling and stitching together the high-magnification ( $10\times$ ) digital images with an automated microscope translation stage commercial software package (Image-Pro MC, Media Cybernetics Inc., Silver Spring, Maryland).

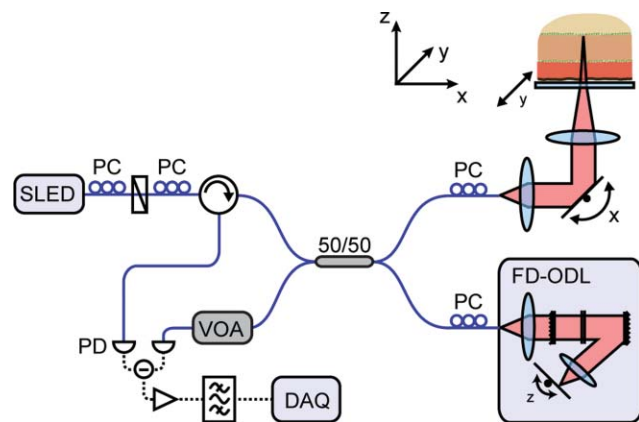


**Fig. 1** Schematic diagram of the fiber-based TD-OCT system: SLED, superluminescent light emitting diode; PC, polarization controller; VOA, variable optical attenuator; FD-ODL, frequency-domain optical delay line; PD, photodetector; DAQ, data acquisition.

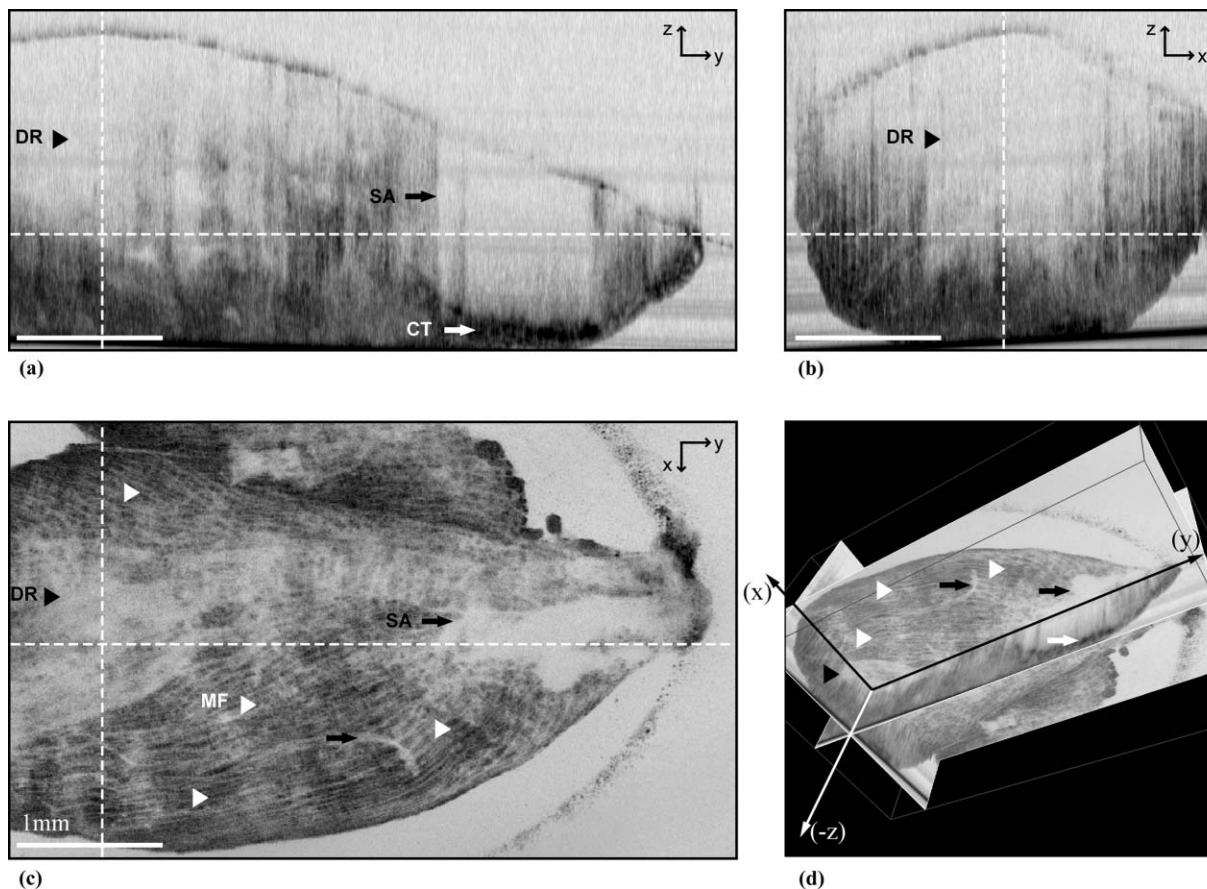


**Fig. 2** OCT image sections from a 3D-OCT dataset of a dystrophic tibialis anterior skeletal muscle from the *mdx* mouse. (a)  $y$ - $z$  OCT plane; (b)  $x$ - $z$  OCT plane; (c) *en face*  $x$ - $y$  OCT plane; (d) rendering of the sections with the axes marked corresponding to the section axes. White dashed lines indicate the sectioning planes. MF, myofibers (white arrowheads); DR, disrupted region (black arrowheads); CT, connective tissue (white arrows); SA, shadow artifact (black arrows). Scale bars 1 mm.

### 3 Results

The results selected for presentation in this section are representative of the 3D-OCT imaging and subsequent H&E- and EBD-histology of 12 skeletal muscle samples taken from five mice. A striated pattern is visible in the *en face*  $x$ - $y$  OCT imaging plane, apparent at all depths ( $z$ -axis) throughout the 3D scan and aligned along the long axis of the muscle sample [Fig. 2(c) and 2(d)]. The orientation of the striation is as expected for myofibers in the sample, and their spacing of 30 to 50  $\mu\text{m}$  (orthogonal to the long axis) is in agreement with accepted values of myofiber diameters.<sup>28</sup>

In some areas of the muscle, circular features can be observed in the B-scan  $x$ - $z$  OCT images, which resemble myofiber-like structures in cross-section. This matches well with the expected orientation of myofibers in the transverse plane and agrees with our previously reported results of OCT images of myofibers in cross-section in muscle autografts.<sup>27</sup> While myofibers can be seen in the OCT B-scan, they are more obvious as the striation pattern seen in the *en face*  $x$ - $y$  OCT images [Fig. 2(c) and 2(d)]. Layered features aligned with the long axis of the muscle sample were also visible in the  $y$ - $z$  plane. The widths of these structures suggest that they are bundles of myofibers (fasciculi) separated by connective tissue (perimysium). The connective tissue of the distal tendon was observed as a highly scattering structure, visible in all three orthogonal planes of the 3D-OCT

dataset [Fig. 2(a) and 2(d)]. It is most obvious in the *en face*  $x$ - $y$  planes, appearing as a highly scattering region containing a regular pattern of circular features. The connective tissue was often observed to cause a shadowing artifact to appear in the tissue layers beneath it due to its strong extinction of the incident light [Fig. 2(a), 2(c), and 2(d)]. The artifact is characterized by low signal, an abrupt change in OCT signal strength with depth following the superficially located strong-scattering structure, and its well-defined boundary in the  $x$ - $z$  and  $y$ - $z$  planes.

A region with a disrupted OCT appearance, lacking the previously described striation pattern, was observed in all three orthogonal planes of the 3D-OCT dataset (Fig. 2). This “disruption region” (DR) is featureless and corrupted by speckle, with low signal and low contrast. However, it lacks the overlying high-scattering structure and the sharp boundaries in the  $x$ - $z$  and  $y$ - $z$  OCT, which characterizes a shadowing artifact.

To investigate this region in more detail, a second scan was obtained by translating the sample along the (positive)  $y$ -axis and generating a 3D-OCT scan that overlapped with the previous data set by 2.5 mm. A representative *en face*  $x$ - $y$  OCT image selected from within the 3D scan is shown in Fig. 3(b). It matches well with the general shape of the sample shown in the photograph [Fig. 3(a)] and with the corresponding H&E- and EBD-histology [Fig. 3(c) and Fig. 3(d), respectively]. The



The H&E-histology of the tibialis anterior muscle sample reveals the characteristics of severe dystropathology [Fig. 3(c)]. There exists a large number of dark-staining inflammatory cells invading the tissue, many degenerating myofibers, and large regions of necrosis and cellular debris. There are very few surviving myofibers present in the sample, which are identified by their peripheral nuclei, intact sarcolemma, and nonfragmented sarcoplasm. Instead, the vast majority of intact fibers are centrally nucleated matured myotubes that have regenerated to form new myofibers following repeated cycles of necrosis and inflammation. A number of regions of muscle necrosis can be seen, identified by the presence of dark-staining (basophilic) inflammatory cells, hypercontracted myofibers, and degenerating necrotic myofibers with fragmented sarcoplasm. This is most obvious in the necrotic lesion (NL) seen in Fig. 3(c). The lesion is visible as a dark-staining large-area feature with a well-defined boundary (black dashed outline). It is characterized by the presence of a high density of invading inflammatory cells, degenerating and necrotic myofibers and their cellular debris, and the presence of fatty and fibrous connective tissue. The necrotic lesion matches well for its location, general size, and shape to the accumulation of EBD observed in the photograph [Fig. 3(a)] and the DR seen in the *en face* OCT image [Fig. 3(b)].

The co-located EBD-histology section further validates the region as a necrotic lesion containing permeable myofibers [Fig. 3(d)]. The accumulation of EBD, visible under fluorescence microscopy as a bright-red area (white dashed outline), indicates the presence of leaky myofibers (pre-necrotic or degenerating) permeable to the EBD-albumin complex. The region of strong EBD-fluorescence matches well with the necrotic lesion identified in the corresponding H&E-histology section.

The outset images [Fig. 3(e)–3(g)] show 4× magnified views of three regions of interest selected from within the tissue: intact myofibers [Fig. 3(E1), 3(F1), and 3(G1)], the interior of the necrotic lesion [Fig. 3(E2), 3(F2), and 3(G2)], and the lesion boundary [Fig. 3(E3), 3(F3), and 3(G3)]. The OCT signature is observed to be different for each region and can be attributed to changes in the tissue structure resulting from dystropathology.

Regions in the OCT data that display the characteristic striation pattern [Fig. 3(E1)] correspond to areas of intact myofibers, as seen in the co-located H&E-histology section [Fig. 3(F1)], which confirms them as regenerated myofibers identified by their central nuclei. This is similar to previously reported results of *en face* images from 3D-OCT imaging corresponding to longitudinal sections of cardiac muscle tissue.<sup>32,38</sup> Hence, the source of the high signal and high contrast striation pattern is optical backscattering from myofibers with intact membranes and sarcoplasm. This is further verified by the lack of EBD accumulation due to the impermeable nature of non-necrotic myofibers, as seen in the corresponding EBD-histology section [Fig. 3(G1)].

The OCT signature in *en face* images from within the lesion is characterized by weak backscattering, low contrast, and a uniform appearance corrupted by speckle, lacking the previously discussed striation pattern [Fig. 3(E2)]. This OCT signature corresponds to the predominant constituents of the lesion identified in the co-located H&E-histology [Fig. 3(F2)]: necrotic myofibers with fragmented sarcolemma and sarcoplasm, a high density of invading inflammatory cells, and fibrous and fatty connective tissue. Within the lesion, a small number of intact

myofibers are present and can be seen in the corresponding OCT image in the lower right section as a feature with higher backscattering. The breakdown of the intact myofiber structure is verified by the red-fluorescence in the EBD-histology image [Fig. 3(G2)], indicating the presence of permeable myofibers (necrotic and/or degenerating) and interstitial space containing connective tissue.

The difference in the OCT signature between intact skeletal muscle tissue and a necrotic lesion, particularly in the *en face* (*x-y*) OCT plane, is further highlighted in the zoomed image of the lesion boundary (black dashed line) [Fig. 3(E3)]. The intact regenerated myofibers with central nuclei clearly gives rise to the striation pattern seen in the left half of the OCT image, while the EBD-positive permeable necrotic myofibers, regions of inflammatory cells, and connective tissue is responsible for the featureless OCT appearance with weak backscattering and low contrast in the right half of the OCT image.

Figure 4 shows another example of identification of a necrotic lesion from 3D-OCT imaging of the gastrocnemus skeletal muscle dissected from the hindlimb of a second treadmill-exercised *mdx* mouse. In the *en face* (*x-y*) OCT image [Fig. 4(b)], we can clearly see the striation pattern due to intact myofibers, as well as the presence of a sickle-shaped DR (white dashed outline), several millimeters in length. The disruption region matches well in its location and shape for the accumulation of EBD in the photograph [Fig. 4(a)]. It is confirmed as a necrotic lesion in the corresponding co-located H&E-histology [Fig. 4(c)] and by the red fluorescence indicating permeable myofibers in the EBD-histology [Fig. 4(d)]. The OCT appearance is highlighted in the 5× zoomed outset images of intact myofibers [Fig. 4(E1), 4(F1), and 4(G1)], the interior of the necrotic lesion [Fig. 4(E2), 4(F2), and 4(G2)], and the lesion boundary [Fig. 4(E3), 4(F3), and 4(G3)].

## 4 Discussion

This study has demonstrated that 3D-OCT has the ability to image, based on intrinsic contrast, individual myofibers and identify necrotic lesions in fresh *ex vivo* samples of skeletal muscles from a mouse model of Duchenne muscular dystrophy.

The striation pattern observed in the *en face* OCT images corresponds to areas of intact fibers, which are clearly seen in the co-located H&E-histology sections as centrally nucleated regenerated myofibers. The source of the OCT appearance is attributed to the presence of the regular alignment of intact myofibers, which is in agreement with previous results reported in *en face* images from 3D-OCT imaging corresponding to longitudinal sections of cardiac muscle tissue.<sup>32,38</sup> The spacing of the myofibers in the OCT images also agrees with accepted values of diameters for myofibers from the tibialis anterior skeletal muscle of the diseased *mdx* mouse. Myofiber diameters range from: 20 to 40  $\mu\text{m}$  at three weeks, 10 to 50  $\mu\text{m}$  at five weeks, and 10 to 130  $\mu\text{m}$  at nine months of age.<sup>28</sup> These measurements were obtained from frozen sections, which undergo less shrinkage than conventional paraformaldehyde fixed and paraffin processed histology sections, and are therefore likely to be more accurate.

In our *y-z* OCT images of fresh *ex vivo* muscle tissue samples, we observed longitudinally oriented fasciculi separated by perimysium. Our results agree with, but were less obvious than,

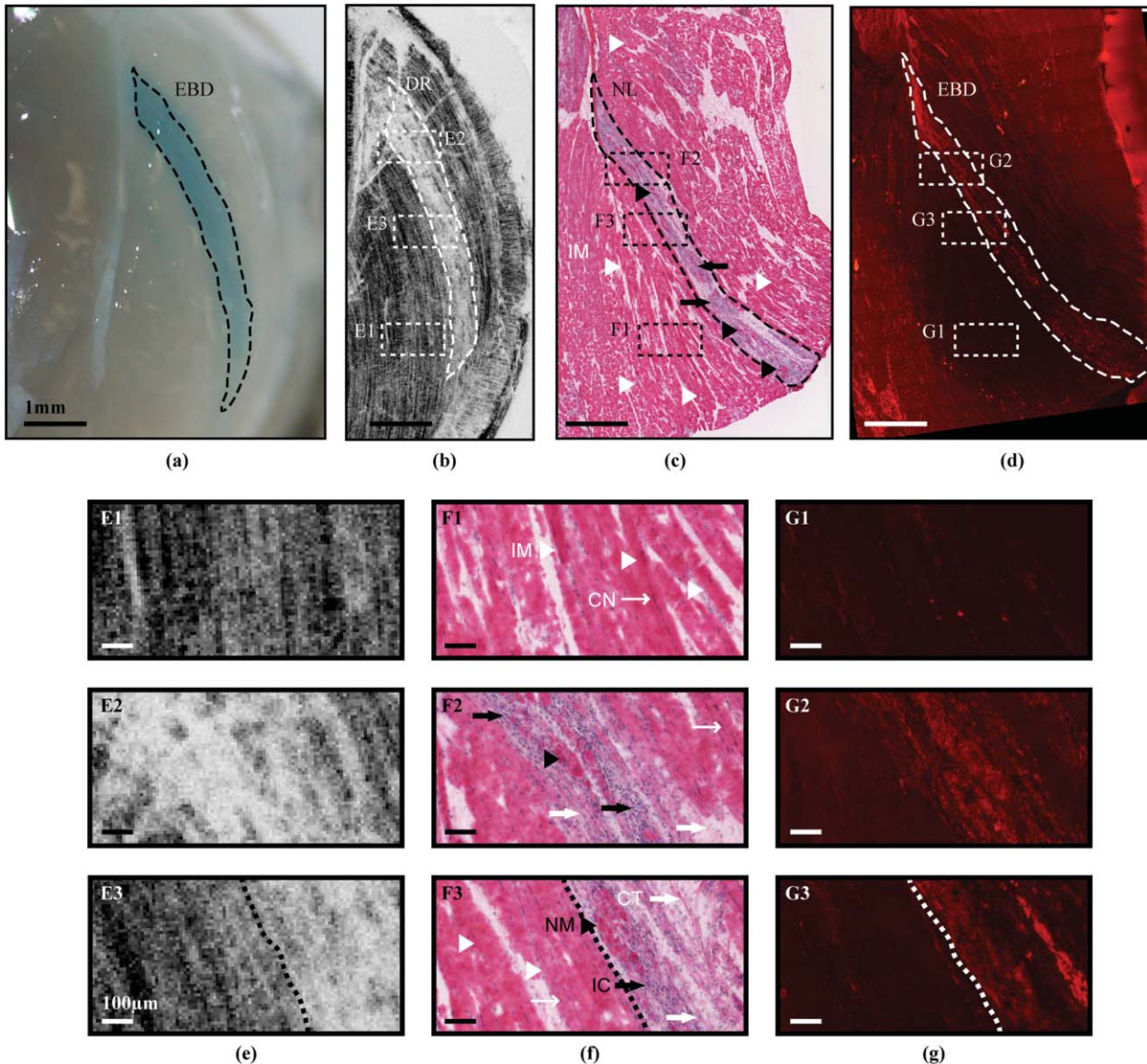


**Fig. 4** Dystrophic gastrocnemius skeletal muscle tissue from a treadmill-exercised *mdx* mouse. (a) Photograph of the posterior surface showing Evans blue dye (EBD) accumulation (bright blue area, dashed outline). (b) *En face* ( $x$ - $y$ ) OCT image displaying the characteristic myofiber striation pattern (MF) (white arrowheads) and a large disruption region of that pattern in the OCT signal (white dashed outline). (c) Corresponding H&E-stained longitudinal histology section showing intact myofibers (MF) (white arrowheads), dystropathology and a large well-defined necrotic lesion, NL (back dashed outline). (d) EBD-fluorescence histology section showing a high accumulation of dye in a large area matching the previously identified necrotic lesion (white dashed outline) (Scale bars 1 mm). The 4 $\times$  magnified view (outsets) show regions of intact fibers (E1, F1, G1), the interior of the necrotic lesion (E2, F2, G2), and the lesion boundary (E3, F3, G3). IM, intact myofibers (white arrowheads); NM, necrotic myofibers (black arrowheads); CT, connective tissue (white arrows); IC, inflammatory cells (black arrows); CN, central nuclei (thin white arrows). Scale bars 100  $\mu$ m.

those presented by Marks et al. from OCT imaging of silicone plastinated skeletal muscle samples.<sup>39</sup> The higher contrast evident in those samples could be attributed to changes in the optical properties of the tissue induced by the plastination method.

In the OCT images, the disrupted region is presented as a featureless area corrupted by speckle that has lost the distinctive striation pattern. It is characterized by low signal and contrast within a relatively well-defined boundary. Three possibilities are advanced to explain the OCT signature: image artifact caused by shadowing, EBD acting as a contrast marker and changing the local optical properties of the tissue, or structural changes of the tissue due to muscle dystropathology. While the disruption region exhibits low signal and low contrast within a well-defined

boundary when viewed in the *en face* ( $x$ - $y$ ) OCT image plane, it lacks two key features that would enable it to be attributed to a shadowing artifact. First, there is no evidence of a strongly scattering structure overlying the region. Second, it does not have sharp boundaries when the 3D-OCT dataset is viewed in depth [ $y$ - $z$ ] and [ $x$ - $z$ ] planes [Fig. 2(a) and 2(b)]. To determine the influence of the Evans blue dye on OCT imaging, separate scattering and absorption experiments were conducted with 1% EBD (w/v) in PBS solution (results not shown). EBD solution in isolation did not generate an OCT backscattering signal above the noise floor and was indistinguishable from that of distilled water. Hence, EBD does not sufficiently backscatter the incident beam at the wavelengths used in the OCT system. To determine

the influence of EBD via absorption of the incident beam, serial dilutions of EBD covering a  $10^4$ -concentration range were mixed with 1- $\mu\text{m}$  diameter polystyrene microspheres and imaged using the OCT system. Addition of differing concentrations of EBD did not attenuate the measured scattering profile of the microsphere solution. Hence, it was found that EBD was not significantly absorbed at the wavelengths used in our system. Thus, EBD does not change the local optical properties of the tissue or act as a contrast agent and is, therefore, not the source of the disruption region in the OCT images. We therefore confirmed that the observed change in the OCT appearance is due to the underlying change in the muscle tissue structure as a result of dystrotopathology, which was validated in the corresponding H&E- and EBD-histology. Comparing the OCT and histology images, it is clear that the necrotic and inflammatory tissue produces less backscatter in OCT images than the surrounding tissue containing intact myofibers, which provided the necessary contrast to visualize the necrotic lesion.

While the morphology evident in the *en face* OCT images presented in this study correlates well with the corresponding histology, OCT is unable to differentiate between pre-necrotic and regenerated myofibers. This discrimination relies on resolving the position of the nucleus with respect to the fiber, as pre-necrotic myofibers have peripheral nuclei while regenerated myofibers have centrally located myofibers. Distinction between the fiber types may still be possible by analyzing the variation in A-scans<sup>40</sup> to determine local optical properties,<sup>41</sup> which could also aid in the identification of necrotic lesions within dystrophic skeletal muscle tissue and the quantitative analysis of their various components.<sup>42</sup>

The utility of future *in vivo* 3D-OCT imaging of mouse skeletal muscle may be limited by the overlying tissue structures, such as skin, and the intrinsic penetration depth of OCT. In this study, we have not imaged through skin. For *in vivo* evaluation of necrotic lesions in mouse models of muscular dystrophy, the generation of high-fidelity OCT images would necessitate direct access to the tissue. This could be achieved using an imaging window, as demonstrated *in vivo* for imaging mice and rabbit alveoli.<sup>43</sup> Alternatively, OCT combined with needle-based imaging probes can penetrate many millimeters into the tissue,<sup>44</sup> as was recently demonstrated *in situ* for imaging sheep lung alveoli.<sup>45</sup>

## 5 Conclusion

This first comprehensive and systematic study shows that 3D-OCT is useful in the structural assessment of pathology and identification of lesions in skeletal muscle tissue from the *mdx* mouse model of Duchenne muscular dystrophy. 3D-OCT is able to image the structural features of interest from skeletal muscle tissue (myofibers, tendon, connective tissue, adipose tissue) based on the intrinsic differences in the scattering properties of these structures. 3D-OCT is able to identify muscle necrosis and lesions, which are identified in scans as regions of low signal, low contrast and a loss of the characteristic striation pattern of intact myofibers. We have also shown that EBD is a suitable *in vivo* marker for targeted 3D-OCT imaging of necrotic lesions and muscle pathology, as it does not interfere with the OCT imaging beam at 1300 nm.

## Acknowledgments

The authors gratefully acknowledge assistance with histological preparation and digital imaging, respectively, from the staff at CellCentral and the Centre for Microscopy, Characterisation and Analysis at The University of Western Australia. We also gratefully acknowledge the technical contribution of the OCT viewing software by Dr. Robert McLaughlin from the Optical + Biomedical Engineering Laboratory and design of the optical source from DenseLight Semiconductors, Singapore. Blake R. Klyen gratefully acknowledges the assistance of the F. S. Shaw Memorial Postgraduate Scholarship.

## References

1. K. Bushby, R. Finkel, D. J. Birnkrant, L. E. Case, P. R. Clemens, L. Cripe, A. Kaul, K. Kinnett, C. McDonald, S. Pandya, J. Poysky, F. Shapiro, J. Tomezsko, and C. Constantin, "Diagnosis and management of Duchenne muscular dystrophy, part 1: diagnosis, and pharmacological and psychosocial management," *Lancet Neurol.* **9**(1), 77–93 (2010).
2. A. Y. Manzur and F. Muntoni, "Diagnosis and new treatments in muscular dystrophies," *Postgrad. Med. J.* **85**(1009), 622–630 (2009).
3. E. Le Rumeur, S. J. Winder, and J.-F. Hubert, "Dystrophin: more than just the sum of its parts," *BBA - Proteins Proteom.* **1804**(9), 1713–1722 (2010).
4. M. J. Spencer and J. G. Tidball, "Do immune cells promote the pathology of dystrophin-deficient myopathies?" *Neuromuscular Disord.* **11**(6–7), 556–564 (2001).
5. J. G. Tidball and M. Wehling-Henricks, "Damage and inflammation in muscular dystrophy: potential implications and relationships with autoimmune myositis," *Curr. Opin. Rheumatol.* **17**(6), 707–713 (2005).
6. N. P. Evans, S. A. Misyak, J. L. Robertson, J. Bassaganya-Riera, and R. W. Grange, "Dysregulated intracellular signaling and inflammatory gene expression during initial disease onset in Duchenne muscular dystrophy," *Am. J. Phys. Med. Rehabil.* **88**(6), 502–522 (2009).
7. T. Shavlakadze, J. White, J. F. Y. Hoh, N. Rosenthal, and M. D. Grounds, "Targeted expression of insulin-like growth factor-1 reduces early myofiber necrosis in dystrophic *mdx* mice," *Mol. Ther.* **10**(5), 829–843 (2004).
8. M. D. Grounds and J. Torrisi, "Anti-TNF $\alpha$  (Remicade<sup>®</sup>) therapy protects dystrophic skeletal muscle from necrosis," *FASEB J.* **18**(6), 676–682 (2004).
9. S. Hodgetts, H. Radley, M. Davies, and M. D. Grounds, "Reduced necrosis of dystrophic muscle by depletion of host neutrophils, or blocking TNF  $\alpha$  function with Etanercept in *mdx* mice," *Neuromuscul. Disord.* **16**(9–10), 591–602 (2006).
10. S. Pierno, B. Nico, R. Burdi, A. Liantonio, M. P. Didonna, V. Cippone, B. Fraysse, J.-F. Rolland, D. Mangieri, F. Andreetta, P. Ferro, C. Camerino, A. Zallone, P. Confalonieri, and A. De Luca, "Role of tumour necrosis factor  $\alpha$ , but not of cyclo-oxygenase-2-derived eicosanoids, on functional and morphological indices of dystrophic progression in *mdx* mice: a pharmacological approach," *Neuropathol. Appl. Neurobiol.* **33**(3), 344–359 (2007).
11. H. G. Radley, M. J. Davies, and M. D. Grounds, "Reduced muscle necrosis and long-term benefits in dystrophic *mdx* mice after cV1q (blockade of TNF) treatment," *Neuromuscul. Disord.* **18**(3), 227–238 (2008).
12. M. D. Grounds, H. G. Radley, G. S. Lynch, K. Nagaraju, and A. De Luca, "Towards developing standard operating procedures for pre-clinical testing in the *mdx* mouse model of Duchenne muscular dystrophy," *Neurobiol. Dis.* **31**(1), 1–19 (2008).
13. K. D. Wallace, J. N. Marsh, S. L. Baldwin, A. M. Connolly, R. Keeling, G. M. Lanza, S. A. Wickline, and M. S. Hughes, "Sensitive ultrasonic delineation of steroid treatment in living dystrophic mice with energy-based and entropy-based radio frequency signal processing," *IEEE Trans. Ultrason. Ferroelectr. Freq. Control* **54**(11), 2291–2299 (2007).
14. D. Laux, H. Blasco, J. Y. Ferrandis, G. Hugon, G. Despau, A. Leydier, and D. Mornet, "In vitro mouse model in Duchenne muscular dystrophy

- diagnosis using 50-MHz ultrasound waves," *Ultrasonics* **50**(8), 741–743 (2010).
15. L. M. McIntosh, R. E. Baker, and J. E. Anderson, "Magnetic resonance imaging of regenerating and dystrophic mouse muscle," *Biochem. Cell Biol.* **76**(2–3), 532–541 (1998).
  16. L. M. McIntosh, K.-E. Granberg, K. M. Briere, and J. E. Anderson, "Nuclear magnetic resonance spectroscopy study of muscle growth, *mdx* dystrophy and glucocorticoid treatments: correlation with repair," *NMR Biomed.* **11**(1), 1–10 (1998).
  17. V. Straub, K. M. Donahue, V. Allamand, R. L. Davisson, Y. R. Kim, and K. P. Campbell, "Contrast agent-enhanced magnetic resonance imaging of skeletal muscle damage in animal models of muscular dystrophy," *Magn. Reson. Med.* **44**(4), 655–659 (2000).
  18. H. Amthor, T. Egelhof, I. McKinnell, M. E. Ladd, I. Janssen, J. Weber, H. Sinn, H.-H. Schrenk, M. Forsting, T. Voit, and V. Straub, "Albumin targeting of damaged muscle fibres in the *mdx* mouse can be monitored by MRI," *Neuromuscul. Disord.* **14**(12), 791–796 (2004).
  19. G. Walter, L. Cordier, D. Bloy, and H. L. Sweeney, "Noninvasive monitoring of gene correction in dystrophic muscle," *Magn. Reson. Med.* **54**(6), 1369–1376 (2005).
  20. M. Kobayashi, A. Nakamura, D. Hasegawa, M. Fujita, H. Orima, and S. Takeda, "Evaluation of dystrophic dog pathology by fat-suppressed T2-weighted imaging," *Muscle Nerve* **40**(5), 815–826 (2009).
  21. J. N. Kornegay, J. A. Li, J. R. Bogan, D. J. Bogan, C. L. Chen, H. Zheng, B. Wang, C. Qiao, J. F. Howard, and X. A. Xiao, "Widespread muscle expression of an AAV9 human mini-dystrophin vector after intravenous injection in neonatal dystrophin-deficient dogs," *Mol. Ther.* **18**(8), 1501–1508 (2010).
  22. M. Bartoli, N. Bourg, D. Stockholm, F. Raynaud, A. Delevacque, Y. Han, P. Borel, K. Seddik, N. Armande, and I. Richard, "A mouse model for monitoring calpain activity under physiological and pathological conditions," *J. Biol. Chem.* **281**(51), 39672–39680 (2006).
  23. S. V. Plotnikov, A. M. Kenny, S. J. Walsh, B. Zubrowski, C. Joseph, V. L. Scranton, G. A. Kuchel, D. Dauser, M. S. Xu, C. C. Pilbeam, D. J. Adams, R. P. Dougherty, P. J. Campagnola, and W. A. Mohler, "Measurement of muscle disease by quantitative second-harmonic generation imaging," *J. Biomed. Opt.* **13**(4), 044018 (2008).
  24. O. Friedrich, M. Both, C. Weber, S. Schurmann, M. D. H. Teichmann, F. von Wegner, R. H. A. Fink, M. Vogel, J. S. Chamberlain, and C. Garbe, "Microarchitecture is severely compromised but motor protein function is preserved in dystrophic *mdx* skeletal muscle," *Biophys. J.* **98**(4), 606–616 (2010).
  25. A. R. Baudy, A. Sali, S. Jordan, A. Kesari, H. K. Johnston, E. P. Hoffman, and K. Nagaraju, "Non-invasive optical imaging of muscle pathology in *mdx* mice using cathepsin caged near-infrared imaging," *Mol. Imaging Biol.* **13**(3), 462–470 (2010).
  26. J. J. Pasquesi, S. C. Schlachter, M. D. Boppart, E. Chaney, S. J. Kaufman, and S. A. Boppart, "In vivo detection of exercise-induced ultrastructural changes in genetically-altered murine skeletal muscle using polarization-sensitive optical coherence tomography," *Opt. Express* **14**(4), 1547–1556 (2006).
  27. B. R. Klyen, J. J. Armstrong, S. G. Adie, H. G. Radley, M. D. Grounds, and D. D. Sampson, "Three-dimensional optical coherence tomography of whole-muscle autografts as a precursor to morphological assessment of muscular dystrophy in mice," *J. Biomed. Opt.* **13**(1), 0111003 (2008).
  28. L. F. B. Torres and L. W. Duchon, "The mutant *mdx*: Inherited myopathy in the mouse. Morphological studies of nerves, muscles and end-plates," *Brain* **110**(2), 269–299 (1987).
  29. G. S. Sandhu, L. Solorio, A.-M. Broome, N. Salem, J. Kolthammer, T. Shah, C. Flask, and J. L. Duerk, "Whole animal imaging," *Wires Syst. Biol. Med.* **2**(4), 398–421 (2010).
  30. B. E. Bouma and G. J. Tearney, Eds., *Handbook of Optical Coherence Tomography* (Marcel Dekker, New York, 2002).
  31. W. Drexler and J. G. Fujimoto, Eds., *Optical Coherence Tomography: Technology and Applications* (Springer, New York, 2008).
  32. W. J. Hucker, C. M. Ripplinger, C. P. Fleming, V. V. Fedorov, A. M. Rollins, and I. R. Efimov, "Bimodal biophotonic imaging of the structure-function relationship in cardiac tissue," *J. Biomed. Opt.* **13**(5), 054012 (2008).
  33. H. G. Radley-Crabb, J. Terrill, T. Shavlakadze, J. Tonkin, P. G. Arthur, and M. D. Grounds, "A single 30 minute treadmill exercise session is suitable for 'proof-of concept studies' in adult *mdx* mice: a comparison of the early consequences of two different treadmill protocols," *Neuromuscul. Disord.* (under review).
  34. J. Terrill, H. G. Radley-Crabb, M. D. Grounds, and P. G. Arthur, "N-acetylcysteine treatment of dystrophic *mdx* mice results in protein thiol modifications and inhibition of exercise induced myofibre necrosis," *Neuromuscul. Disord.* (under review).
  35. P. W. Hamer, J. M. McGeachie, M. J. Davies, and M. D. Grounds, "Evans blue dye as an *in vivo* marker of myofibre damage: optimising parameters for detecting initial myofibre membrane permeability," *J. Anat.* **200**(1), 69–79 (2002).
  36. A. V. Zvyagin, E. D. J. Smith, and D. D. Sampson, "Delay and dispersion characteristics of a frequency-domain optical delay line for scanning interferometry," *J. Opt. Soc. Am. A* **20**(2), 333–341 (2003).
  37. R. Matsuda, A. Nishikawa, and H. Tanaka, "Visualization of dystrophic muscle-fibers in *mdx* mouse by vital staining with Evans blue: evidence of apoptosis in dystrophin-deficient muscle," *J. Biochem.* **118**(5), 959–964 (1995).
  38. C. P. Fleming, C. M. Ripplinger, B. Webb, I. R. Efimov, and A. M. Rollins, "Quantification of cardiac fiber orientation using optical coherence tomography," *J. Biomed. Opt.* **13**(3), 030505 (2008).
  39. D. L. Marks, E. J. Chaney, and S. A. Boppart, "Plastinated tissue samples as three-dimensional models for optical instrument characterization," *Opt. Express* **16**(20), 16272–16283 (2008).
  40. R. A. McLaughlin, L. Scolaro, P. Robbins, C. Saunders, S. L. Jacques, and D. D. Sampson, "Parametric imaging of cancer with optical coherence tomography," *J. Biomed. Opt.* **15**(4), 046029 (2010).
  41. C. Y. Xu, J. M. Schmitt, S. G. Carlier, and R. Virmani, "Characterization of atherosclerosis plaques by measuring both backscattering and attenuation coefficients in optical coherence tomography," *J. Biomed. Opt.* **13**(3), 034003 (2008).
  42. F. J. van der Meer, D. J. Faber, J. Perree, G. Pasterkamp, D. B. Sassoon, and T. G. van Leeuwen, "Quantitative optical coherence tomography of arterial wall components," *Lasers Med. Sci.* **20**(1), 45–51 (2005).
  43. J. Bickenbach, R. Dembinski, M. Czaplak, S. Meissner, A. Tabuchi, M. Mertens, L. Knels, W. Schroeder, P. Pelosi, E. Koch, W. Kuebler, R. Rossaint, and R. Kuhlen, "Comparison of two *in vivo* microscopy techniques to visualize alveolar mechanics," *J. Clin. Monit. Comput.* **23**(5), 323–332 (2009).
  44. Y. Wu, J. Xi, L. Huo, P. Jason, E. J. Shin, S. A. Giday, A. M. Lennon, M. I. F. Canto, J. H. Hwang, and X. Li, "Robust high-resolution fine OCT needle for side-viewing interstitial tissue imaging," *IEEE J. Sel. Top. Quantum Electron.* **16**(4), 863–869 (2010).
  45. B. C. Quirk, R. A. McLaughlin, A. Curatolo, R. W. Kirk, P. B. Noble, and D. D. Sampson, "In situ imaging of lung alveoli with an optical coherence tomography needle probe," *J. Biomed. Opt.* **16**(3), 036009 (2011).